Atmospheric
Measurement
Techniques

# Ground-based all-sky mid-infrared and visible imagery for purposes of characterizing cloud properties

**D. I. Klebe**[1,4]**, R. D. Blatherwick**[2,4]**, and V. R. Morris**[3]

[1]Denver Museum of Nature and Science, Denver, Colorado, USA
[2]University of Denver, Denver, Colorado, USA
[3]Pacific Northwest National Laboratory, Richland, Washington, USA
[4]Solmirus Corporation, Woodland Park, Colorado, USA

*Correspondence to:* D. I. Klebe (dimitri.klebe@dmns.org)

**Abstract.** This paper describes the All Sky Infrared Visible Analyzer (ASIVA), a multi-purpose visible and infrared sky imaging and analysis instrument whose primary function is to provide radiometrically calibrated imagery in the mid-infrared (mid-IR) atmospheric window. This functionality enables the determination of diurnal fractional sky cover and estimates of sky/cloud temperature from which one can derive estimates of sky/cloud emissivity and cloud height. This paper describes the calibration methods and performance of the ASIVA instrument with particular emphasis on data products being developed for the meteorological community. Data presented here were collected during the Solmirus' ASIVA campaign conducted at the Atmospheric Radiation Measurement (ARM) Southern Great Plains (SGP) Climate Research Facility from 21 May to 27 July 2009. The purpose of this campaign was to determine the efficacy of IR technology in providing reliable nighttime sky cover data. Significant progress has been made in the analysis of the campaign data over the past several years and the ASIVA has proven to be an excellent instrument for determining sky cover as well as the potential for determining sky/cloud temperature, sky/cloud emissivity, precipitable water vapor (PWV), and ultimately cloud height.

# 1 Introduction

Uncertainty in the characterization of clouds in general circulation models (GCMs) is one of the major causes of the broad range of future climate change predictions (US DOE, 2010). Fractional sky cover, which is closely related to cloud fraction (a dominant modulator of radiative fluxes), has been an integral part of the observational data set that feeds these GCMs (Kassianov et al., 2005). Currently, however, sky cover is only directly determined at the Atmospheric Radiation Measurement (ARM) sites during daytime hours utilizing the Total Sky Imager (TSI) (Long et al., 2001). Other indirect cloud fraction data products can be derived from surface radiometers (Long et al., 2006a) and the statistical analysis of lidar and radar observations (Qian et al., 2012). A direct means of determining nighttime sky cover has been and remains a critical programmatic gap in ARM's observational data set and is an important factor in understanding the life cycle of clouds, one of the central themes of the Atmospheric System Research program. The mid-infrared (mid-IR) atmospheric window from 8–13 micrometers (μm) has long been known to hold great promise in closing this gap as well as providing other valuable ground-based cloud properties and atmospheric data (Shaw et al., 2005; Thurairajah and Shaw, 2005). A thermal IR imager has the distinct advantage of directly detecting emission from clouds, rather than relying on scattered light or obscured starlight, and is not hampered by the presence of the Sun or the Moon, thus providing consistent and reliable information under a wide variety of conditions.

Significant work has been done in determining sky cover using all-sky imagers that operate in the visible spectrum (Pfister et al., 2003; Heinle et al., 2010; Calbó and Sabburg, 2008; Cazorla et al., 2008; Huo and Lu, 2009). All-sky imagers that operate in the mid-IR (Liu et al., 2011; Feister et

**Fig. 2.** All-sky images acquired on 25 May 2009 at 23:07 UTC (top) and 21 July 2009 at 14:17 UTC (bottom). Images shown are from the TSI instrument (left), the ASIVA visible camera (middle), and from ASIVA's 10.2–12.2 μm IR channel (right).

al., 2010) have thus far been limited to instruments that scan or acquire multiple images to create all-sky images. These instruments are met with unique calibration challenges. The ASIVA instrument circumvents many of these issues by the use of an all-sky lens and, as will be described in this paper, is integral to the calibration process.

This paper will discuss the ASIVA instrument with particular emphasis on the calibration procedures that have been developed to improve mid-IR radiometric performance enabling the removal of water vapor emission. Infrared data analysis procedures that are being developed to characterize cloud properties with particular emphasis on determining sky cover will also be discussed. In addition, sky cover data from ASIVA's visible channel will be discussed and compared to data from the infrared channel as well as from the TSI.

## 2 Description of the ASIVA instrument

The ASIVA instrument (shown in Fig. 1) was deployed at the ARM Southern Great Plains (SGP) site (36.605° N, 97.485° W, 318 m) for an infrared sky imager field campaign from 21 May to 27 July 2009. This instrument was a prototype unit that featured an infrared camera subsystem consisting of a $320 \times 256$ uncooled microbolometer array sensitive to 8–14 μm radiation, a 180° (all-sky) custom-designed hard-carbon-coated waterproof lens, and a filter wheel which included the two IR filters. The IR camera provided image data at 14-bit resolution and at a 30 Hz rate. Sixteen of these images were co-added to produce a single frame with an effective exposure of 0.53 s. Sixteen consecutive frames were then bundled to produce a 3-dimensional (data cube) FITS (Flexible Image Transport System) file that was stored to disk for future data analysis. The ASIVA visible camera subsystem featured a color progressive scan $2048 \times 1536$ CMOS
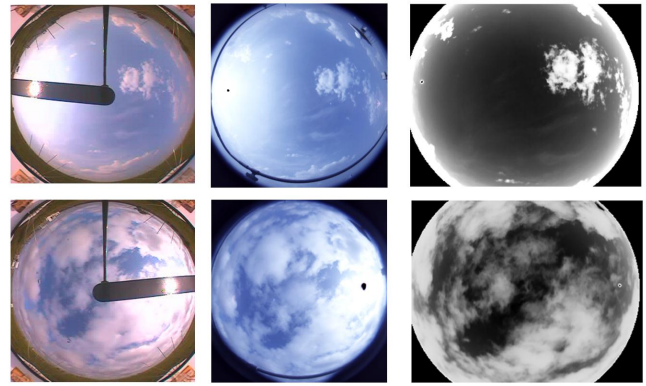
detector array and a 180° off-the-shelf lens. The visible camera provided image data at 10-bit resolution per color and exposures up to 2 min in duration. The instrument featured a unique hatch/radiation shield subsystem used for radiometric calibration. The hatch subsystem provided the following relevant features: (1) integration of the IR blackbody reference and visible dark reference into a single hatch mechanism. (2) IR blackbody reference and the visible reference remained in the same protected orientation (pointed downward) as the hatch mechanism was opened and closed. (3) Temperature sensor and a heater were embedded in the IR blackbody reference to provide in situ radiometric image calibration. (4) Radiation shield allowed the blackbody reference to equilibrate with the ambient air temperature.

An observing script governed the data acquisition process which determined what filters and exposure times were to be used for each 5 min data sequence. Each sequence began with the hatch closed. An IR blackbody reference image (in each of the two filters) and a visible dark reference image were acquired in the closed position. The hatch was then opened wherein one visible and two infrared sky images were acquired until the next data acquisition sequence. All data sequences were identical with the exception of toggling the exposure time for the visible camera between a daytime and nighttime setting. All data were stored to disk.

A collection of images acquired on 25 May 2009 at 23:07 UTC and 21 July 2009 at 14:17 UTC is shown in Fig. 2. Images from the ARM facility's TSI instrument are shown for comparison with ASIVA's visible camera along with one of ASIVA's IR channels. Note that the ASIVA visible images do not utilize a sun occulter and that the camera's 10-bit-per-color resolution (TSI uses 8 bit per color) allows for better sensitivity near the Sun. The ASIVA IR images are single frame (0.53 s exposure) images and demonstrate that the Sun's presence has almost no impact on the image.

Compare Modtran Simulation with ASIVA Response Curves
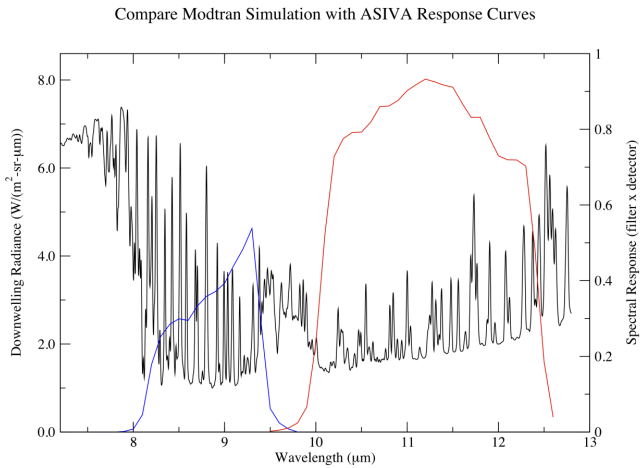


**Fig. 3.** Simulated clear-sky downwelling radiance for 22 mm PWV pointed at the zenith. Spectral response of two ASIVA filters (red and blue) used in this research.

A major challenge for thermal imagers has been separating the effects of water vapor emission from those of cloud emission, particularly cirrus clouds (Brocard et al., 2011). The ASIVA's primary function is to provide radiometrically calibrated imagery across the entire sky in the mid-IR. Figure 3 shows the clear-sky downwelling radiance as simulated using MODTRAN (MODerate resolution atmospheric TRANsmission; Berk et al., 1999) for a standard mid-latitude summer atmosphere (Anderson et al., 1986) pointed at the zenith with the $CO_2$ mixing ratio set to 380 ppmv and the $H_2O$ profile scaled to 22 mm of precipitable water vapor (PWV), typical of conditions found at the ARM SGP site. Absorption, and therefore thermal emission, is dominated by water vapor at wavelengths less than 8 μm, by carbon dioxide at wavelengths greater than 13 μm, and by ozone near 9.5 μm. Water vapor absorption lines are present throughout this spectral interval but are least prevalent in the 10.2–12.2 μm region. For this reason, a custom 10.2–12.2 μm filter for optimizing clear-sky–cloud contrast was fabricated for the ASIVA instrument. The spectral response of this filter (shown in red) as well the 8.25–9.25 μm filter (shown in blue) used in this research are presented in Fig. 3.

## 3 Infrared radiometric calibration

### 3.1 Determination of instrument response coefficients

A somewhat more detailed discussion of the ASIVA's calibration procedure can be found in Klebe et al. (2012). In the interest of completeness, much of that discussion is repeated here. The ASIVA instrument incorporates a two-step calibration process in determining the spectral radiance for IR images. The first step in this calibration procedure is to determine the instrument response coefficients $G_\lambda$ for every

pixel in the array in each IR filter. These coefficients are generated using Eqs. (1) and (2).

$$G_\lambda = \frac{I_\lambda}{\epsilon_\lambda \cdot BB_\lambda(T)} \left\{ \frac{Counts}{Watts/m^2/\mu m/sr} \right\}, \quad (1)$$

where $I_\lambda$ is instrumental counts measured for the blackbody reference in a specific filter, $\epsilon_\lambda$ is emissivity of the blackbody reference in a specific filter, and

$$BB_\lambda(T) = \quad (2)$$

$$\int \frac{1.19 \times 10^8 \cdot \lambda^{-5}}{e^{1.44 \times 10^4 / \lambda T} - 1} t_\lambda d\lambda \bigg/ \int t_\lambda d\lambda \left\{ Watts/m^2/\mu m/sr \right\},$$

where $t_\lambda$ is system response as a function of wavelength for a specific filter.

The blackbody spectral density equation $BB_\lambda(T)$ above assumes a wavelength λ in μm and is integrated over the system response $t_\lambda$ (which includes the combined effects of filter/lens transmission and nominal IR detector sensitivity as a function of wavelength) for a particular temperature $T$ in Kelvin. The emissivity $\epsilon_\lambda$ of the blackbody depends on the coating and design of the calibration reference used to cover the IR lens. The emissivity is assumed to be constant for a given filter but can be adjusted from one filter to the next if necessary. A value of 0.95 was used for this study.

To eliminate instrumental offsets, $G_\lambda$ was determined by calculating a least squares linear fit to the $I_\lambda$ versus $\epsilon_\lambda \cdot BB_\lambda(T)$ data for a range of temperatures. The built-in blackbody reference located inside the hatch cover was used to determine the instrumental response of the system and also to measure the fixed pattern components in the image during data acquisition. A temperature sensor was bonded within the blackbody reference and the temperature data were written into the FITS header when acquiring images. A heater was embedded in the blackbody reference and was used to control its temperature during calibration.

The calibration procedure was performed on 21 May 2009. During the procedure, the hatch was opened and the blackbody was heated to ∼ 80 °C and then allowed to passively cool down to near-ambient temperature. During the cooldown period, the hatch was periodically closed (2 min intervals) to take calibration data in each of the two IR filters. Data were acquired in this fashion for approximately 60 minutes wherein the hatch stayed open for the majority of the time to prevent heating of the IR lens during the calibration procedure. The data were analyzed as described above and a calibration image file containing the $G_\lambda$ values for each pixel was created. An example of the calibration data set used to establish $G_\lambda$ for a single central pixel (representative of every pixel in the array) for the 10.2–12.2 μm filter is provided in Fig. 4. The response is linear over a factor of two in radiance, yielding great confidence in extrapolating to low radiance values as is done when observing clear skies with low PWV.
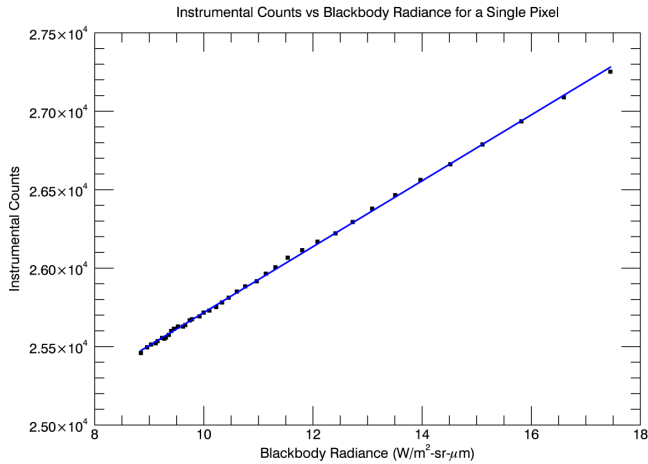
**Fig. 4.** 10.2–12.2 μm instrument response for a single central pixel.

## 3.2 Calibration of spectral radiance images

The second step in the calibration procedure is to determine the sky's spectral radiance ($F_{\lambda \mathrm{Sky}}$) for a given filter using Eq. (3).

$$F_{\lambda \mathrm{Sky}} = \frac{I_{\lambda \mathrm{Sky}} - I_{\lambda \mathrm{Ref}}}{G_\lambda} + \mathrm{BB}_\lambda \left(T_{\mathrm{Ref}}\right) \left\{ \mathrm{Watts/m^2/\mu m/sr} \right\}, \qquad (3)$$

where $I_{\lambda \mathrm{Sky}}$ is instrumental counts measured for the sky image, $I_{\lambda \mathrm{Ref}}$ is instrumental counts measured for the reference blackbody image, $G_\lambda$ is instrument response coefficients derived from Eq. (1), and $\mathrm{BB}_\lambda (T_{\mathrm{Ref}})$ is integrated blackbody radiance derived from Eq. (2) for ambient temperature $T_{\mathrm{Ref}}$.

For purposes of the analysis presented in Sect. 4, we define the normalized spectral radiance $\mathcal{F}_{\lambda \mathrm{Sky}}$ given by Eq. (4). $\mathcal{F}_{\lambda \mathrm{Sky}}$ can be thought of as a proxy to the sky's average emissivity. $\mathcal{F}_{\lambda \mathrm{Sky}}$ is generally an underestimate of the true emissivity since the ambient temperature given by $T_{\mathrm{Ref}}$ is nominally greater than the mean temperature of the emitting sky.

$$\mathcal{F}_{\lambda \mathrm{Sky}} = {F_{\lambda \mathrm{Sky}}}\big/ {\mathrm{BB}_\lambda \left(T_{\mathrm{Ref}}\right)}. \qquad (4)$$

## 4 Cloud detection and fractional sky cover analysis

### 4.1 Verification of calibration procedures

The calibration procedures described in Sect. 3 provide the foundation for cloud detection and other cloud data products that can be derived from the ASIVA instrument. As a verification of these procedures, ASIVA spectral radiance data were compared with the precisely calibrated data retrieved from the Atmospheric Emitted Radiance Interferometer (AERI) instrument (Knuteson et al., 2004) available for the campaign period. The mean spectral radiance was determined by averaging the AERI spectral radiance data over the response of each of the two ASIVA IR channels. The 8 min

average AERI data were utilized, as this cadence was similar to the 5 min cadence used by the ASIVA instrument. Calibrated ASIVA data were then evaluated at the zenith, coincident with AERI's field of view. Comparison plots of AERI data with ASIVA data for the two daytime periods that will be highlighted in this paper are shown in Fig. 5. Agreement is very good ($< 5\,\%$) for the two daytime comparisons, which are representative of the entire campaign data set. Note that the agreement is good in both clear and cloudy circumstances. Discrepancies (e.g., 25 May 2009, 17:00 UTC) are likely due to slight differences in the beam size and direction utilized by each instrument.

### 4.2 Removal of clear-sky emission

The primary step in the cloud detection process is to remove the effects of clear-sky emission. This is done by employing the all-sky capabilities of the ASIVA instrument. Figure 6 illustrates the procedure in which the clear-sky normalized radiance is determined from the ASIVA IR image data set. In Fig. 6, the normalized radiance pixel data are plotted as a function of airmass for the images shown in Fig. 2. The normalized radiance data are sorted into 29 airmass bins of roughly equal pixel count. The lower envelope of points in each airmass bin (shown as red squares) is fit to a 2nd-order polynomial equation (blue line), which identifies the clear-sky radiance. Even in the very cloudy image of 21 July 2009 at 14:17 UTC, the lower envelope is still well defined (chi-square $= 0.0005$) and serves as an excellent representation of the underlying clear-sky emission. The clear-sky emission is then described as a function of airmass utilizing this polynomial equation and is then subtracted from the original normalized radiance image to yield the clear-sky subtracted images.

The clear-sky subtracted images form the basis of sky cover determination. A cloud/no-cloud decision can be simply made by choosing a single threshold value, above which an individual pixel is determined to be cloudy. For this study, two thresholds were used to determine the presence of "low-emission" and "high-emission" clouds. The ultimate goal is to explore if one can identify threshold values that correlate well with the "thin" and "opaque" criteria employed by the TSI instrument (Long et al., 2006b). The advantage of expressing the clear-sky subtracted image in normalized radiance is that as mentioned it is related to the emissivity of the cloud and therefore the threshold values should be largely independent of ambient temperature.

One of the primary challenges of producing a robust cloud decision map is determining the clear-sky radiance in nearly 100 % cloudy conditions. This is accomplished by demanding that the chi-square value for the polynomial fit be less than some threshold (chosen to be 0.002 in this analysis) to ensure a strict goodness-of-fit criterion. If this criterion is not met, the previous polynomial equation that has met this
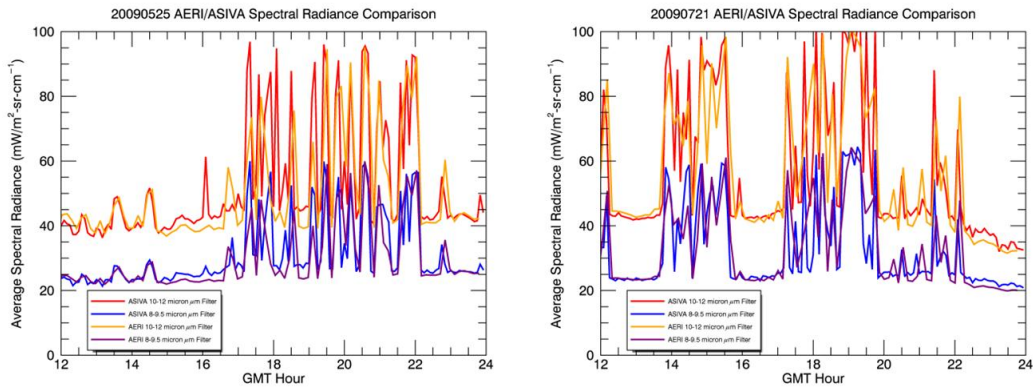
**Fig. 5.** Comparison of AERI with ASIVA spectral radiance data in each of the two filters for **(a)** 25 May 2009 and **(b)** 21 July 2009.
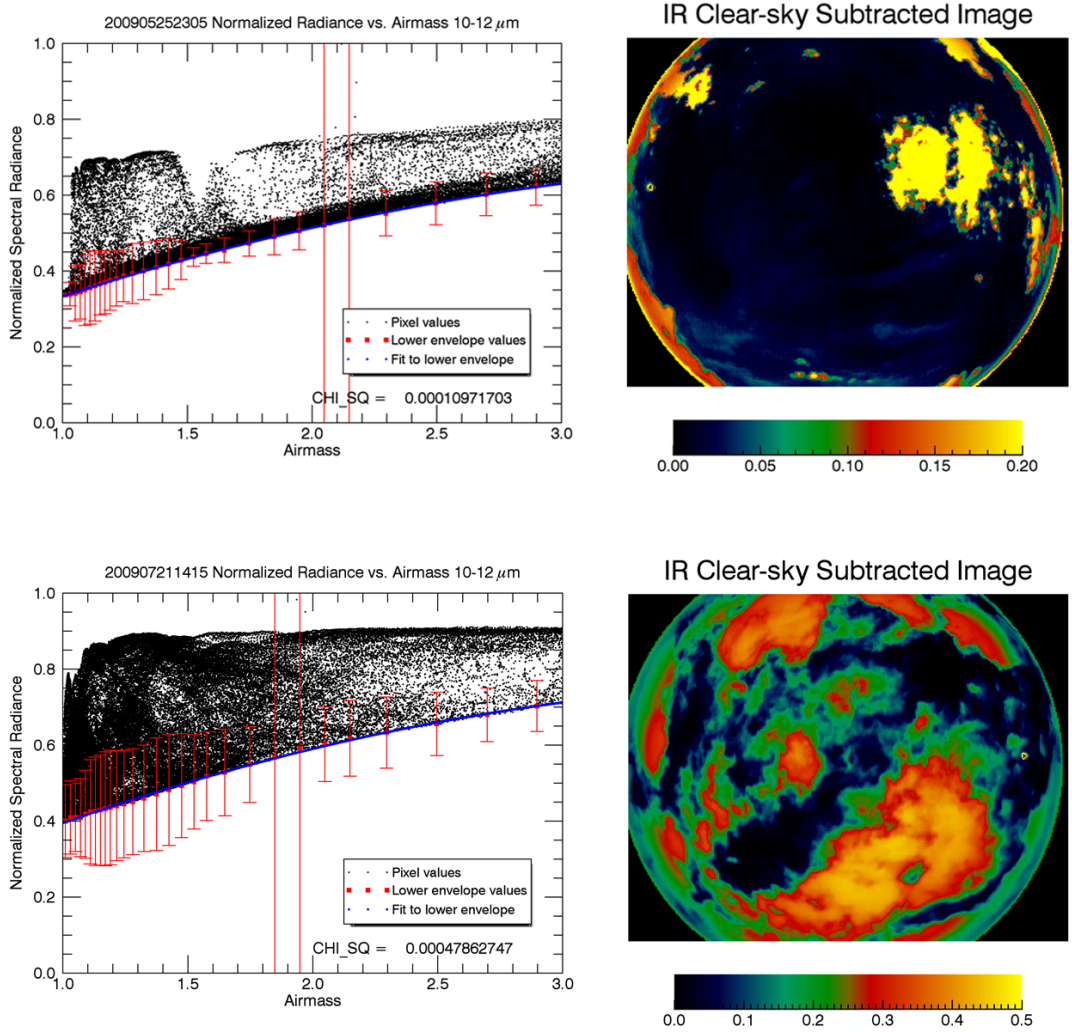


**Fig. 6.** Pixel normalized radiance vs. airmass data (left) on 25 May 2009 at 23:07 UTC (top) and 21 July 2009 at 14:17 UTC (bottom). Blue line represents 2nd-order polynomial fit to lower envelope of points (red squares) in each of 29 airmass bins. Clear-sky subtracted images derived from this analysis (right). Note: image is truncated at 6 airmasses. Large error bars (near 2 airmasses) are due to the Sun's extreme pixel values at this location.

criterion is used to define the clear-sky radiance. We have found this procedure to be very effective.

## 4.3 Fractional sky cover determination

After determining the clear-sky emission, cloud decision masks can be processed by applying thresholds to the clear-sky subtracted images. Figure 7 shows fractional sky cover comparisons between TSI (thin and opaque) and ASIVA IR (low and high emission) during daylight hours for the 25 May and 21 July 2009 data sets. Agreement between TSI data and the ASIVA IR data are excellent; however, different low-emission threshold values were used for the two days. Threshold values (in normalized radiance units) of $0.15 <$ low-emission cloud $< 0.05$ and high-emission cloud $\geq 0.05$ were used for the 25 May data set, and $0.03 <$ low-emission cloud $< 0.05$ and high-emission cloud $\geq 0.05$ for the 21 July data set. The TSI data used in this comparison were improved from those available from the ARM archive using a more sophisticated analysis package (Long, 2010). This analysis is used to improve the reliability of the TSI instrument for low Sun elevation angles.

The 21 July data set is dominated by thick opaque clouds. The 25 May data set, which provided a mix of thin and opaque clouds, represents more challenging conditions for sky cover analysis. The difficulty arises in that the emission from the thin cirrus clouds evident in Fig. 6 is only slightly above the clear-sky radiance. As can be seen in Fig. 7, much better agreement between low-emission and thin clouds is achieved by reducing the lower end of the low-emission threshold to 0.015. However applying this analysis to the 21 July data set would produce a larger fraction of low-emission clouds than shown in Fig. 7. This discrepancy is due to the fact that the cloud decision analysis is fundamentally different between the IR and visible. The TSI measures optical thickness of a cloud and the ASIVA IR channel measures cloud emission. However, the primary goal of this research has been to obtain as close an agreement as possible between the TSI and ASIVA's IR channel. The entire 2009 campaign data set will be used to determine the best correlation between these sky cover measurements.

## 4.4 Retrieval of fractional sky cover data product from ASIVA visible data

Retrieval of the sky cover data product from ASIVA's visible channels uses the same analysis adopted by the TSI instrument. The analysis involves taking the ratio of the red image to blue image and then setting appropriate opaque/thin/no-cloud thresholds (Long et al., 2006b). Figure 8 shows the visible red/blue ratio images coincident with the images shown in Fig. 2. The Sun has been occulted in software (the larger circle) and is similar in size to the zone of avoidance utilized in the TSI cloud fraction analysis. In addition, a small circle is used to mask an artifact seen at the Sun's position reflected

through the zenith. This artifact (which can be seen in Fig. 2) is brought about by internal reflection within the fisheye lens. Since the ASIVA instrument does not require a sun occulter like that utilized in the TSI instrument, eliminating this part of sky is relatively minor in the analysis.

Thresholds are then set to define the thin and opaque boundaries to provide the best agreement with the TSI instrument. Figure 9 shows the sky cover analysis for the 25 May and 21 July data sets. The ASIVA visible channel performs very well for low Sun angles without any further processing. The agreement is remarkably good and demonstrates that the ASIVA visible subsystem is more than adequate in reproducing TSI daytime functionality. Development of ASIVA's sky cover data product is nearly complete and is currently being applied to the entire field campaign data set.

## 5 Sky/cloud temperature and other potential ASIVA data products

As a radiometrically calibrated instrument the ASIVA has the potential of delivering many other data products that will be useful to the meteorological community. This section discusses the current research in this area.

## 5.1 Determination of sky/cloud temperature

Two temperature data products can be immediately derived from ASIVA's IR radiance data: brightness temperature and color temperature. The brightness temperature (for a given IR filter) of an image can be determined by equating the measured radiance with a blackbody whose temperature yields this same radiance. Brightness temperature images determined from the representative images of 25 May (surface temperature 304 K) and 21 July (surface temperature 297 K) are shown in Fig. 10. Note that the peripheries of the clouds indicate lower brightness temperature consistent with lower optical depth in these regions.

The color temperature can be inferred by taking the ratio of sky radiance images acquired in the 8.25–9.25 μm and 10.2–12.2 μm filters and assigning this a temperature for which a blackbody yields this same radiance ratio. Color temperature has the distinct advantage of only being affected by differences in sky/cloud emissivity in the two filters but is insensitive to the total optical depth. For this reason we believe that color temperature will ultimately yield a better measure of the true temperature for optically thin clouds. Color temperature images are also shown in Fig. 10. The color temperature images show variations (both positive and negative temperature fluctuations) at the periphery of the clouds due to the motion of the clouds over the data acquisition period. This is particularly evident in the 21 July image as the clouds were very fast moving. Current ASIVA instruments now acquire 8.25–9.25 μm and 10.2–12.2 μm image data in a much shorter time interval to combat this problem. Also note that
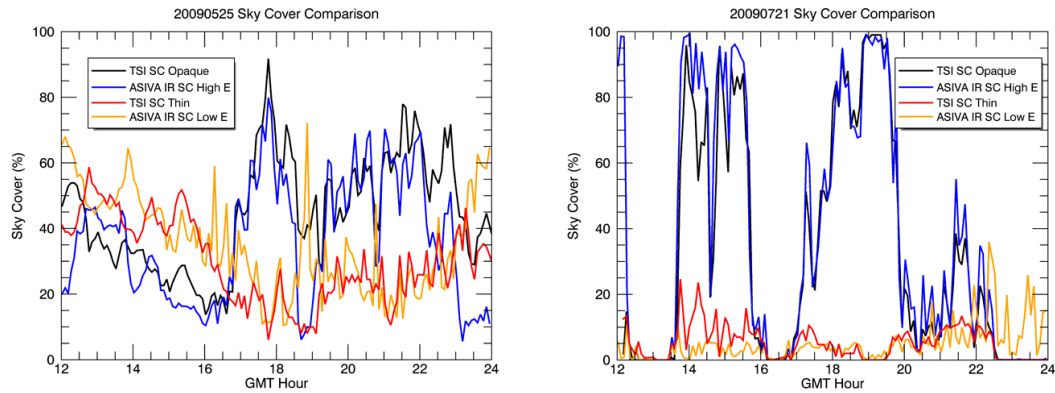
**Fig. 7. (a)** Sky cover comparisons between TSI (thin and opaque) and ASIVA IR (low and high emission) during daylight hours on 25 May 2009 for threshold values 0.15 < low emission < 0.05 and high emission ≥ 0.05, and **(b)** on 21 July 2009 for threshold values 0.03 < low emission < 0.05 and high emission ≥ 0.05.
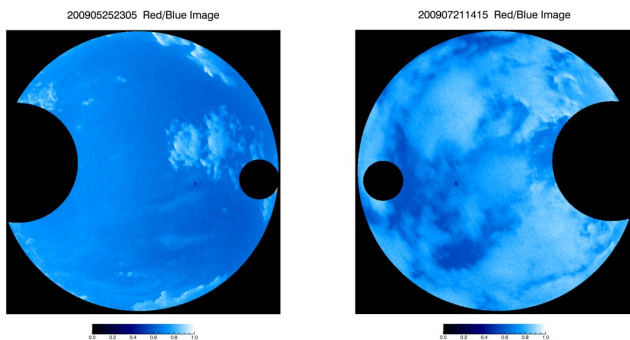


**Fig. 8. (a)** Red / blue ratio image for 25 May 2009. **(b)** Red / blue ratio image for 21 July 2009.

the clear-sky color temperature is higher (one would expect lower temperatures) at the zenith due to sky emissivity differences in the two IR filters.

Brightness and color temperatures are similar in the optically thick regions of clouds, indicating cloud temperatures 10–20 K below the ground temperature. To some degree, these color maps already provide an estimate of cloud temperature that may be very valuable to cloud modelers. To improve on the accuracy of this measurement, one will have to account for the intervening atmospheric absorption and emission in each of the filters. This is where knowledge of PWV (discussed in Sect. 5.3) is required to provide additional information regarding the atmosphere's radiative properties.

## 5.2 Determination of sky/cloud emissivity

Perhaps one of the most powerful data products that can be derived using the temperature analysis outlined above is an accurate estimate of the emissivity of an image. By assuming that the color temperature is indeed a measure of the true mean temperature for an image, one can compute

a blackbody radiance image from the color temperature image. By dividing the measured radiance by the blackbody radiance derived from the color temperature, one arrives at a measure of the emissivity of the sky. Figure 10 also shows the results of this analysis.

The accuracy of this measure is somewhat hampered by the variations in emissivity between the two IR filters but can be corrected using knowledge of the PWV burden and the information it yields regarding the atmosphere's radiative properties. Ignoring the effects of cloud motion, the images of Fig. 10 show cloud emissivity near unity for opaque clouds as one would expect. They also show the expected variations in clear-sky emissivity (i.e., lower emissivity at the zenith and higher emissivity near the horizon).

## 5.3 Determination of precipitable water vapor (PWV)

As discussed above, determination of PWV is important as it can provide valuable ancillary information in the analysis of other cloud property data products, in particular refining cloud temperature measurements. The basic analysis strategy is to compare the clear-sky envelope (described in Sect. 4.2) with modeled data. The model data are constructed using a series of MODTRAN simulations that provide a parameterization of the normalized clear-sky downwelling radiance as a function of PWV evaluated at different elevation angles (i.e., airmass). Preliminary simulations have been run for each of ASIVA's filters using a radiosonde data set acquired for 21 July 2009. The simulated data set is then best fit to the clear-sky envelope determined for a particular image, thus providing an estimate of PWV. Figure 11 shows the result of this analysis for the 25 May and 21 July data sets. The PWV data are compared with data retrieved from the microwave radiometer (MWR), an instrument with accuracy of better than 1 mm PWV. The correlation is reasonable for the 21 July data set (the day from which the radiosonde data were used in the MODTRAN analysis) but deviates significantly for the
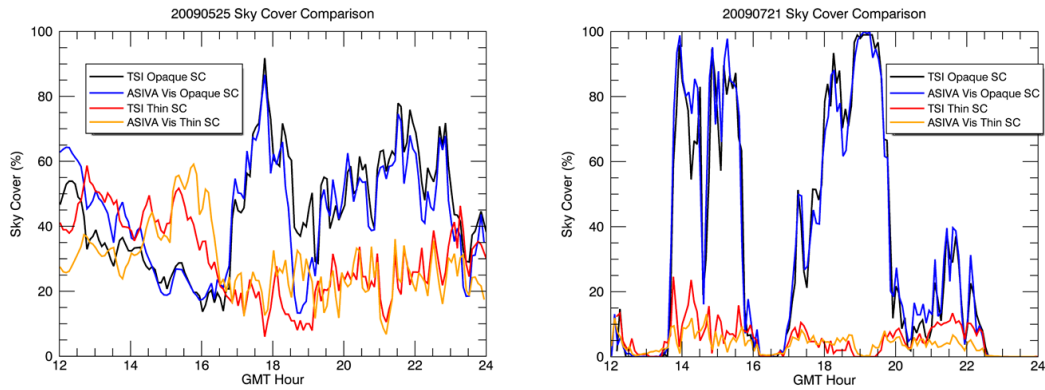
**Fig. 9. (a)** Sky cover comparisons between TSI and ASIVA visible for opaque and thin cloud types for 25 May 2009 and **(b)** 21 July 2009.
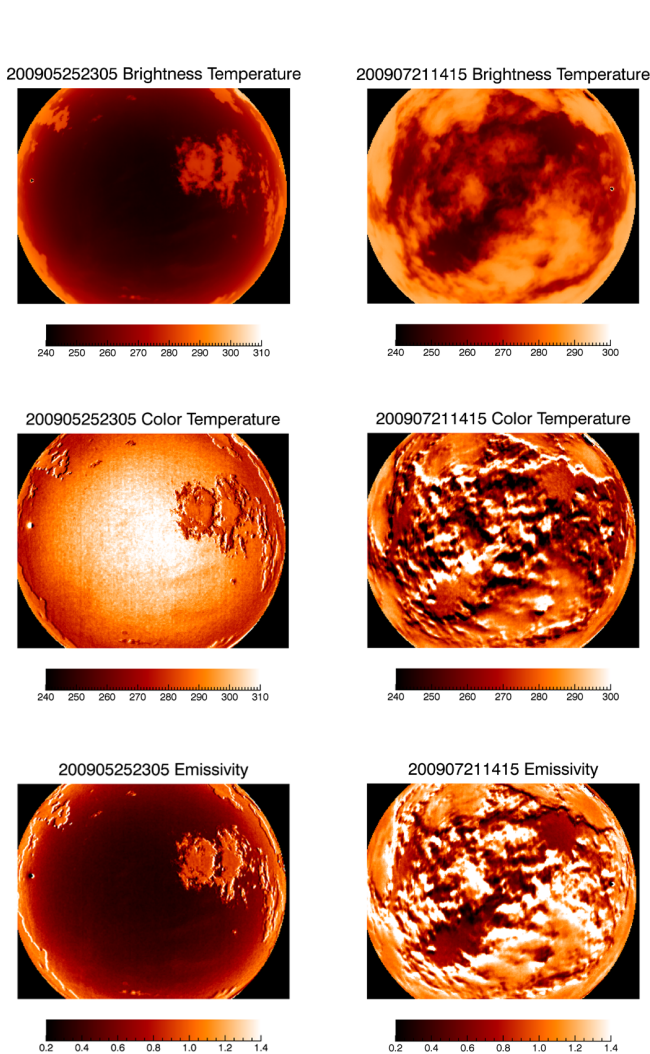


**Fig. 10.** Brightness temperature (K, top), color temperature (middle), and emissivity (bottom) for representative images for 25 May 2009 (left) and 21 July 2009 (right).
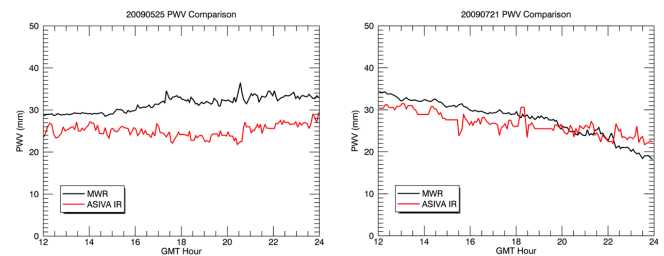


**Fig. 11.** Comparison of MWR with ASIVA PWV data for **(a)** 25 May 2009 and **(b)** 21 July 2009.

25 May data set. This suggests coincidental radiosonde data may be required to improve the accuracy of ASIVA's estimate of PWV.

Better accuracy in the determination of PWV may not be required in that this measure is only required to make second-order corrections to data products such as the sky/cloud temperature and emissivity images. If better accuracy is required, other instruments such as MWR could be used in a value-added product (VAP). Ultimately, we wish to obtain a measure of cloud temperatures with accuracy sufficient to provide a useful estimate of cloud height. Cloud height can be estimated from ASIVA cloud temperature data by utilizing the altitude versus temperature information retrieved from radiosonde data. Validation of this technique would be accomplished by comparison to cloud height measurements retrieved from the ARM ceilometer (CEIL) operated at SGP during the campaign period. This is the subject of future research.

## 6 Conclusions

The ASIVA demonstrates considerable promise in providing a diurnal fractional sky cover data product. ASIVA sky cover data (both IR and visible) correlate very well with daytime data retrieved from the Total Sky Imager. Radiometric

calibration procedures have been validated by data retrieved from the Atmospheric Emitted Radiance Interferometer. The quality of the ASIVA's radiometric data promises to yield additional products such as quality estimates of sky/cloud temperature (both color and brightness temperature), sky/cloud emissivity, precipitable water vapor, and ultimately cloud height.

# References

Anderson, G. P., Clough, S. A., Kneizys, F. X., Chetwynd, J. H., and Shettle, E. P.: AFGL Atmospheric ConstituentProfiles (0–120 km), AFGL-TR-86-0110, available at: http://www.dtic.mil/dtic/tr/fulltext/u2/a175173.pdf (last access: 19 February 2014), 1986.

Berk, A., Anderson, G. P., Bernstein, L. S., Acharya, P. K., Dothe, H., Matthew, M. W., Adler-Golden, S. M., Chetwynd, J. H., Richtmeier, S. C., Pukall, B., Alfred, C. L., Jeong, L. S., and Hoke, M. L.: Modtran4 radiative transfer modeling for atmospheric correction, P. Soc. Photo-Opt. Ins., 3756, 348–353, 1999.

Brocard, E., Schneebeli, M., and Mätzler, C.: Detection of Cirrus Clouds Using Infrared Radiometry; IEEE T. Geosci. Remote., 49, 595–602, 2011.

Calbó, J. and Sabburg, J.: Feature Extraction from Whole-Sky Ground-Based Images for Cloud-Type Recognition, J. Atmos. Oceanic Technol., 25, 3–14, 2008.

Cazorla, A., Olmo, F. J., and Alados-Arboledas, L.: Development of a sky imager for cloud cover assessment, J. Optical Soc. Am. A, 25, 29–39, 2008.

Feister, U., Möller, H., Sattler, T., Shields, J., Görsdorf, U., and Güldner, J.: Comparison of macroscopic cloud data from ground-based measurements using VIS/NIR and IR instruments at Lindenberg, Germany, Atmos. Res., 96, 395–407, 2010.

Heinle, A., Macke, A., and Srivastav, A.: Automatic cloud classification of whole sky images, Atmos. Meas. Tech., 3, 557–567, doi:10.5194/amt-3-557-2010, 2010.

Huo, J. and Lu, D.: Cloud Determination of All-Sky Images under Low-Visibility Conditions, J. Atmos. Ocean. Technol., 26, 2172–2181, 2009.

Kassianov, E., Long, C. N., and Ovtchinnikov, M.: Cloud Sky Cover versus Cloud Fraction: Whole-Sky Simulations and Observations, J. Appl. Meteorol., 44, 86–98, 2005.

Klebe, D., Sebag, J., Blatherwick, R. D., and Zimmer, P. C.: All-Sky Mid-Infrared Imagery to Characterize Sky Conditions and Improve Astronomical Observational Performance, Publ. Astron. Soc. Pac., 124, 1309–1317, 2012.

Knuteson, R. O., Revercomb, H. E., Best, F. A., Ciganovich, N. C., Dedecker, R. G., Dirkx, T. P., Ellington, S. C., Feltz, W. F., Garcia, R. K., Howell, H. B., Smith, W. L., Short, J. F., and Tobin, D. C., Amospheric Emitted Radiance Interferometer, Part I: Instrument Design, J. Atmos. Ocean. Technol., 21, 1763–1776, 2004.

Liu, L., Sun, X., Chen, F., Zhao, S., and Gao, T.: Cloud Classification Based on Structure Features of Infrared Images, J. Atmos. Ocean. Technol., 28, 410–417, 2011.

Long, C. N.: Correcting for Circumsolar and Near-Horizon Errors in Sky Cover Retrievals from Sky Images, Atmos. Sci. J., 4, 45–52, 2010.

Long, C. N., Slater, D. W., and Tooman, T.: Total Sky Imager (TSI) Model 880 Status and Testing Results, Atmospheric Radiation Measurement Program Technical Report, ARM TR-004, 2001.

Long, C. N., Ackerman, T. P., Gaustad, K. L., and Cole, J. N. S.: Estimation of Fractional Sky Cover from Broadband Shortwave Radiometer Measurements, J. Geophys. Res., 111, D11204, doi:10.1029/2005JD006475, 2006a.

Long, C. N., Sabburg, J. M., Calbó, J., and Pagès, D.: Retrieving Cloud Characteristics from Ground-Based Daytime Color All-Sky Images, J Atmos. Ocean. Technol., 23, 633–652, 2006b.

Pfister, G., McKenzie, R. L., Liley, J. B., Thomas, A., Forgan, B. W., and Long, C. N.: Cloud coverage based on all-sky imaging and its impact on the surface solar irradiance, J. Appl. Meteor., 42, 1421–1434, 2003.

Qian, Y., Long, C. N., Wang, H., Comstock, J. M., McFarlane, S. A., and Xie, S.: Evaluation of cloud fraction and its radiative effect simulated by IPCC AR4 global models against ARM surface observations, Atmos. Chem. Phys., 12, 1785–1810, doi:10.5194/acp-12-1785-2012, 2012.

Shaw, J. A., Nugent, P. W., Pust, N. J., Thurairajah, B., and Mizutani, K.: Radiometric cloud imaging with an uncooled microbolometer thermal infrared camera, Opt. Express, 13, 5807–5817, 2005.

Thurairajah, B. and Shaw, J. A.: Cloud statistics measured with the infrared cloud imager (ICI), IEEE T. Geosci. Remote, 43, 2000–2007, 2005.

US DOE: Atmospheric System Research (ASR) Science and Program Plan, US Department of Energy, Washington, DC, available at: http://science.energy.gov/~/media/ber/pdf/Atmospheric_system_research_science_plan.pdf (last access: 19 February 2014), 2010.